



HAL
open science

Visualization and Characterization of Heterogeneous Water Flow in Double-Porosity Media by Means of X-ray Computed Tomography Porous media

Z. Peng, Céline Duwig, P. Delmas, Jean-Paul Gaudet, A. Gastelum Strozzi, P. Charrier, H. Denis

► **To cite this version:**

Z. Peng, Céline Duwig, P. Delmas, Jean-Paul Gaudet, A. Gastelum Strozzi, et al.. Visualization and Characterization of Heterogeneous Water Flow in Double-Porosity Media by Means of X-ray Computed Tomography Porous media. *Transport in Porous Media*, 2015, pp.art. 0572. 10.1007/s11242-015-0572-z . ird-01202110

HAL Id: ird-01202110

<https://ird.hal.science/ird-01202110>

Submitted on 18 Sep 2015

HAL is a multi-disciplinary open access archive for the deposit and dissemination of scientific research documents, whether they are published or not. The documents may come from teaching and research institutions in France or abroad, or from public or private research centers.

L'archive ouverte pluridisciplinaire **HAL**, est destinée au dépôt et à la diffusion de documents scientifiques de niveau recherche, publiés ou non, émanant des établissements d'enseignement et de recherche français ou étrangers, des laboratoires publics ou privés.

Visualization and Characterization of Heterogeneous Water Flow in Double-Porosity Media by Means of X-ray Computed Tomography

Z. Peng¹ · C. Duwig^{1,2} · P. Delmas³ · J. P. Gaudet¹ ·
A. Gastelum Strozzi⁴ · P. Charrier⁵ · H. Denis¹

Received: 25 March 2014 / Accepted: 4 September 2015
© Springer Science+Business Media Dordrecht 2015

Abstract Three-dimensional visualization of dynamic water transport process in soil by computed tomography (CT) technique is still limited by its low temporal resolution. In order to monitor dynamically water transport in soil, a compromise has to be found between water flow velocity and CT acquisition time. Furthermore, an efficient image analysis method is necessary. In this work, we followed the water transport in three dimensions by CT imaging across a double-porosity media constituted of two distinct materials, i.e. sand and porous clay spheres. The CT acquisition parameters were adjusted to the water pore velocity so that we succeeded to register the water front displacement per time range of 25 min. We also used the image subtraction method to extract water distribution evolution with time with a space resolution of 6×10^{-3} cm. Both time and space resolution are relatively high compared with other dynamic studies. The water content profiles showed that the clay spheres remained in their dry state during water infiltration, while the water transport only occurred in the sand matrix. These results are consistent with macroscopic experiments. The water front visualized by CT showed a non-symmetrical shape which was related to water transfer in non-equilibrium as shown by column displacement experiments.

Keywords 3D visualization · Water transport · Computed tomography · Image analysis · Porous media

✉ C. Duwig
celine.duwig@ird.fr

¹ IRD/UJF-Grenoble 1, LTHE UMR 5564, BP 53, Grenoble Cedex 9, France

² LTHE, Bâtiment OSUG-B, Domaine universitaire, BP 53, 38041 Grenoble Cedex 09, France

³ Department of Computer Science, The University of Auckland, PB 92019, Auckland, New Zealand

⁴ UNAM, CCADET, Ciudad Universitaria, 04510 Mexico Cuidad, Mexico

⁵ UJF-Grenoble 1, 3SR UMR 5521, BP 53, Grenoble Cedex 9, France

1 Introduction

Understanding water flow transport in porous media is a central issue to natural and engineered soil science. Groundwater and vadose zone flow, contaminant transfer, and energy-related activities such as geothermal energy production depend on the transport properties at pore scale. To study the water transport properties in porous media, traditional methods exist such as water retention (Schjonning et al. 2005; Holtham et al. 2007) and mercury intrusion curves (Lugato et al. 2009) to estimate pore size distribution, or infiltration experiments to estimate hydraulic conductivity (Angulo-Jaramillo et al. 2000). However, these macroscopic techniques have some important drawbacks. These techniques are based on the hypothesis that pores are represented by parallel tubes of different diameters. In the case of water retention and mercury intrusion curves, they cannot provide an estimation of the pore shape as the total porosity is calculated as the sum of accessible pores from the intrusion of the liquid (mercury or water) so that unconnected pores are not detected.

Computed tomography (CT) of X-rays or neutrons provides reliable information at microscale of porous media morphology (Sleutel et al. 2008; Luo et al. 2010; Dal Ferro et al. 2012; Elyeznasni et al. 2012; Munkholm et al. 2012), multi-phase determination of stationary, or transient flow (Hopmans et al. 1992; Wildenschild et al. 2005; Schaap et al. 2008; DiCarlo et al. 2010; Akhtar et al. 2011; Sammartino et al. 2012). According to equipment resolution and sample size, individual grains and fluid interfaces at pore scale can be achieved by CT. Furthermore, many physical and chemical phenomena occur at this scale and determine soil characteristics and transport properties at macroscale.

One particular interest to apply CT is to observe transport phenomena across heterogeneous unsaturated porous media to better understand the impact of porous structure (pore size, connectivity and porosity) on water transport properties. Indeed, the temporal and spatial distribution of water in soil resulting from heterogeneous water flow is affected by the soil structure, i.e. the spatial arrangement of its constituents. When the materials constituting the porous media differ in size and hydraulic properties, the water distribution and flow paths can reveal high complexity. However, the role played by the geometry of solid and voids and the hydraulic properties of the different constituents is still unclear (Vogel and Roth 2003). Since the CT techniques are able to visualize simultaneously the spatial and temporal distribution of solid and liquid phases in 3D (Heindel et al. 2008; Wildenschild and Sheppard 2013), this latter seems to be a good approach to overcome the lack of knowledge. Only a few authors performed spatio-temporal studies of soil behaviour using CT technologies (Schaap et al. 2008; Vasin et al. 2008; Kneafsey et al. 2011; Sammartino et al. 2012). This is both due to the trade-off between acquisition time and image quality and resolution creating a difficult balance between low temporal resolution and acceptable spatial resolution. Consequently, most studies of water transport in transient states were based on 2D radiography (Hopmans et al. 1992; Maruyama et al. 2003; Carminati et al. 2007, 2008; DiCarlo et al. 2010; Esser et al. 2010). Hopmans et al. (1992) studied water infiltration during one-step outflow experiments on repacked homogeneous samples of a sandy soil. Maruyama et al. (2003) recorded the movement of soil water occurring in an Andosol sample using X-ray with a liquid contrast agent. However, the effect of the contrasting agent on the fluid physical and chemical properties and its flow pattern compared to pure water was not discussed. Carminati et al. (2007, 2008) monitored the water exchange in 3D between wet and dry aggregates and simulated the observed water flow and water content distribution with Richards equation using synchrotron-based X-ray tomographic microscopy.

64 The 3D measurement of water content distribution in heterogeneous sands during multi-
65 step drainage cycles was reported by [Schaap et al. \(2008\)](#) and [Vasin et al. \(2008\)](#). The later
66 used a combination of “fast” 2D neutron transmission tomography to image relatively “slow
67 transient drainage processes” (at a resolution of 0.027 cm and an acquisition time of 20 s)
68 combined with computed tomography to compute a 3D mapping of the studied sample (at
69 the same spatial resolution for an acquisition time of 2 h). [Kneafsey et al. \(2011\)](#) proposed an
70 indirect analysis method by observation of density changes of CT signals caused by hydrate
71 formation and water flowing in samples of methane-hydrate bearing sand. [Sammartino et al.](#)
72 [\(2012\)](#) used a medical four-slice helical computed tomography to attain fast acquisition of 2D
73 slices at 0.0625 cm thickness. This method provides new quantitative information on pref-
74 erential flow processes occurring in an unsaturated undisturbed soil as well as demonstrates
75 the potential for the dynamic imaging of infiltration experiments. However, several obstacles
76 in image quality persist such as low signal-to-noise ratio due to low energy of medical X-ray
77 tomography (to protect the patients) and loss of water detection due to low spatial resolution
78 as typical of commercial medical imaging apparatus.

79 To our knowledge, a dynamic approach of the 3D visualization of water flow at the micro-
80 scopic and macroscopic scales (defined as pore scale and sample scale respectively) based
81 on a compromise between spatial and temporal resolution in unsaturated porous media has
82 still not been achieved. Under this context, the goal of this work was to monitor and charac-
83 terise the 3D water flow path by computed tomography (CT) during dynamic experiments at
84 microscale spatial resolution at regular temporal increments. The CT study in a natural soil
85 reveals many difficulties such as large amount of diverse constituents, low scanned porosity
86 compared with total porosity, and large heterogeneity. As a proof of concept, the natural soil
87 was replaced by a known double-porosity media constituted of spheres made of sintered clay
88 (intra-aggregate pores at nanometre scale) and sand (inter-aggregate pores at micrometre
89 scale). The presence of two different porous media (sand and porous clay spheres) leads to a
90 heterogeneity in structure and impacts hydraulic properties. Consequently, different dynamic
91 processes at local scale between the two pore systems influence the macroscopic behaviour of
92 the media ([Lewandowska et al. 2004](#)). Water transport in double-porosity media, by numeric
93 and experimental approaches, has been extensively studied by Lewandowska and colleagues
94 ([Lewandowska et al. 2004, 2005a,b, 2008](#); [Szymkiewicz et al. 2008](#); [Szymkiewicz and](#)
95 [Lewandowska 2008](#)). They observed that the macroscopic behaviour of the double-porosity
96 media was mainly affected by the degree of heterogeneity of pores (local geometry and
97 conductivity contrast). Nevertheless, their numeric modelling with experimental results was
98 only validated at macroscopic scale and the kinetics at microscopic scale was not checked.
99 To overcome this lack of knowledge, we worked on the visualization and characteriza-
100 tion of heterogeneous water flow in a double-porosity media at the microscale interface
101 (6×10^{-3} cm resolution) by means of X-ray computed tomography from an initial state (dry
102 state) to a saturated state (fully wet) following a infiltration experience. The objective was:
103 (i) to demonstrate the feasibility of CT technique to visualize water flow through heteroge-
104 neous porous media in 3D, (ii) to develop an adequate image analysis technique for image
105 acquired at different water content conditions, and (iii) to characterize water flow in the two
106 medium. The developed methodology in this study allows visualizing and characterizing the
107 3D water flow at water pore velocity in the range of saturated hydraulic conductivity of fine
108 sand.

2 Material and Methods

2.1 Sample Preparations

2.1.1 Material Characterization

The double-porosity (DP) media are a physical model composed of sintered clay spheres (biolite: ceramic shell with honeycomb core produced by firing natural clay to temperatures of 1100–1200 °C in a rotating kiln) and Hostun sand (HN34). Mineralogical composition of Hostun sand is mainly quartz ($\text{SiO}_2 > 98\%$, Desaunay 2011). Its granulometry was characterized by laser diffractometry (Mastersize, Malvern), and its mean grain diameter was 0.0275 cm with a relatively uniform grain size distribution. The total porosity of sand after packing was around 0.43 (see Table 1).

The clay spheres porosity was determined by mercury porosimetry (AutoPore IV 9500, Micromeritics). Connected porosity was 0.445 with media intra-aggregate pore size 4×10^{-6} cm. Solid and bulk densities of sintered clay spheres were also determined by mercury porosimetry with values of 2.38 and 1.32 g cm^{-3} respectively. Average diameter of clay spheres is 0.5 ± 0.1 cm. The permeability was estimated from mercury intrusion curves through the XDQ code (Xu et al. 1997) with value of $3.3 \times 10^{-12} \text{ cm}^2$ which corresponds to a hydraulic conductivity of $3.23 \times 10^{-7} \text{ cm s}^{-1}$ for water. This value is six times smaller than that of clay spheres used in Lewandowska et al. (2008) and Tran Ngoc (2008).

2.1.2 Column

The double-porosity media (previously dried during 24h at 105 °C) were filled into a glass column (inner diameter 2.6 cm and height 10 cm, Fig. 1b), by packing the two constituents (sand and clay spheres) in a periodic manner (Fig. 1a) following Lewandowska et al. (2008) and Tran Ngoc (2008). The spheres were carefully arranged by hand in a homogeneous distribution for each layer. Voids between spheres were filled by sand. This process was repeated by placing layer by layer up to fill the whole column (Fig. 1b). Although the spheres and their packing were not completely homogeneous, the average height of the periodic arrangement was 0.87 cm, as controlled by porosity determination from CT scan (twice the distance between porosity maximum on Fig. 1c). Three columns were built up each with an equal weight fraction of sand and clay spheres (Table 2). The total porosity of the DP column was calculated to be around 0.44 whereas the visible porosity at CT scan resolution and pixel averaging was on average 0.18.

2.2 Infiltration Experiment and Setup

The set-up representation is shown in Fig. 1d. The column was vertically connected to a water inlet at the top side and an outlet at the bottom side. At each side, the double-porosity media were maintained by a rigid grid covered with a porous membrane. The boundary condition at inlet, i.e. the water flow rate, was controlled by a peristaltic pump which was connected to a water tank for water supply. The water tank was closed to avoid water evaporation. A constant capillary pressure head of -60 cm was imposed at the base of the column, and the leachates returns to the water tank. The weight evolution of water tank was monitored by a Mettler Toledo microbalance connected to a computer. The maximum error of observations was 0.01 g, which corresponds to an accuracy of ± 0.002 cm height of water. The room temperature varied between 23 and 24 °C.

Table 1 Physical characteristics of the two media

Medium	Elementary particle size (cm)	Skeleton specific density (g cm ⁻³)	Dry bulk density (g cm ⁻³)	Mean porosity	Pore sizes (cm)	Ks, hydraulic conductivity at saturation (cm s ⁻¹)
HN34 sand	0.0275	2.66 ^a	1.51	0.43	-	~3 × 10 ⁻⁵
Sintered clay spheres	0.4-0.6	2.38	1.32	0.45 ^b	4 × 10 ^{-6b}	3.23 × 10 ^{-7c}
Double-porosity media	-	-	1.44	0.44	-	-

^a Obtained from [Desaunay \(2011\)](#)

^b Intra-aggregate pores, obtained by mercury porosimetry

^c Obtained with XDQ model ([Xu et al. 1997](#))

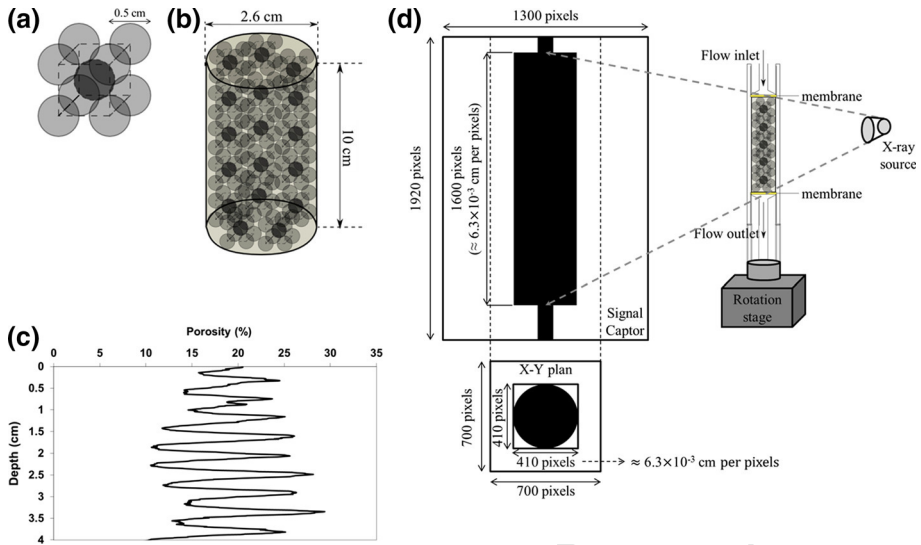


Fig. 1 **a** Geometric representation of clay spheres arrangement; **b** schematic representation of column size; **c** evolution of porosity as determined by CT scan (for pores $> 6.3 \times 10^{-3}$ cm) with depth; **d** schematic representation of infiltration setup and its installation in CT measurements

151 Assuming the weight loss in the water tank is equal to the weight gain in soil column
 152 (without taking into account the water volume in capillaries), this latter provides the deter-
 153 mination of water content evolution of the soil column as a function of time during transient
 154 regime.

155 Before initiating the dynamic CT imaging experiment, three water flows were tested in soil
 156 columns with identical geometry to estimate water infiltration travel time in the soil column.
 157 Before each infiltration, the porous media were initially kept air-dry, and the quantity of each
 158 media (sand and clay spheres) was separately measured with the microbalance before packing
 2 in column. The details of infiltration experience for each column are showed in Table 2.

159 The dispersivity coefficient of the double-porosity (DP) media was determined during a
 160 tracer displacement experiment in column 1, at Darcy water velocity of 6.59×10^{-4} cm s^{-1} .
 161 When the water flow reached the steady state, a pulse of KBr solution (670 mg Br l^{-1}) of
 162 around 1.1 pore volume was injected at the top of the column. The pore volume is defined
 163 as the volume of water in the column at steady state. Leachates were collected at the bottom
 164 of the column every 5 min, and Br concentration was analysed with ionic chromatog-
 165 raphy (Metrohm). Convection–dispersion transport parameters were determined from the Br
 166 breakthrough curve using the CXTFIT 2.1 code (Toride et al. 1999) in inverse mode. A
 167 homogeneous HN34 sand column was studied in the same set-up for comparison, with the
 168 same Darcy velocity, KBr solution, and injected pore volume, and the only difference was
 169 the leachates collection time (every 10 min).
 170

171 2.3 CT Scanner Acquisition Parameters

172 The infiltration experiment was dynamically imaged using X-ray tomography technologies
 173 (TomRX solutions) in the 3SR (Soils, Solids, Structures and Risks) Laboratory, Grenoble,
 France. The CT scan equipment is calibrated one during the day prior to initiating exper-

Table 2 Details of column constitution and parameters for infiltration experiences

	Sand weight (g)	Clay spheres weight (g)	Darcy flow (cm s ⁻¹)	Time range of water front displacement (min)	Theoretical inter-aggregate porosity ^a	Measured water content ^b (cm ³ cm ⁻³)
Column1	38.5	36.7	6.59×10^{-4}	~46	0.186	0.174
Column2	36.7	37.6	2.83×10^{-4}	~108	0.179	0.174
Column3	38.1	38	6.41×10^{-5}	~474	0.181	0.179

^a Porosity between sand grains, and between sand grains and clay spheres

unaccepted proof

174 iments. The calibration object consisted of a set of vertically aligned lead spheres which
 175 are image with the same CT parameters as our samples, which are later input in the CT
 176 reconstruction software. Later the infiltration set-up was installed, and the core column was
 177 aligned to the X-ray beams in order to maximize the signal gain onto the captor. The sensor
 178 size is of 1300 by 1920 pixels. In order to scan the whole column, the distance from source
 179 to objet was adjusted so that the sensor height captured the entire column height, i.e. 1600
 180 pixels for a height of 10 cm, which leads to a spatial resolution of 6.3×10^{-3} cm in all three
 181 dimensions.

182 Computed tomography generates a three-dimensional image of the inside structure of
 183 the studied porous media by acquiring two-dimensional X-ray images (N) taken around a
 184 single (vertical) axis of rotation (Herman 2009). To reduce the signal-to-noise ratio, each
 185 final 2D radiographic image is usually computed as the average of n images acquired at the
 186 same angular position. Given our experimental constraints, a compromise must be made to
 187 minimize the radiographic images acquisition time while maintaining a balanced signal-to-
 188 noise ratio and 3D reconstruction accuracy. The acquisition time T is given by the following
 189 equation:

$$T = N \times n \times \tau \quad (1)$$

191 where N is the angular increment onto a defined angular section between 0 and 360° ; n is
 192 the amount of repetition per angular position for the averaging process; τ is the pause time
 193 between two image captures at the same angle.

194 By performing different tests, the optimal CT acquisition parameters to ensure suitable
 195 image quality and acquisition time were found as followed: the value of N was fixed at 1200
 196 for all the scans onto an angular section of 360° . The value of n which determines the noise
 197 level was fixed at 8. The value of τ for a significant signal acquisition was adjusted at 0.1 s
 198 (10 images per second) for all the scans.

199 The photon energy of X-rays (the spot energy) depends on the generator excitation. The
 200 relationship between transmission coefficient of each media (gas, liquid, and solid) and
 201 photon energy is different: low photon energy leads to high transmission coefficient contrast
 202 that allows better distinguishing different media, but low photon transmission due to low
 203 photon energy requires long acquisition time. High photon energy leads to high photon
 204 transmission and short acquisition time resulting in reduced transmission coefficient contrast
 205 (Markowicz 1993). Accordingly, we did set for the whole experiment a tension of 100 kV and
 206 a current of 300 μ A to excite the generator as the best compromise to distinguish between
 207 water and sand.

208 This CT parameter configuration led to a temporal resolution of around 25 min per scan
 209 (refer to a full 360° tomography acquisition). The pore velocity of water was slowed down
 210 to achieve a travel time significantly higher than 25 min. In column 3, we used a low water
 211 flow rate (3.4×10^{-5} $\text{cm}^3 \text{s}^{-1}$, which corresponds to a Darcy velocity of 6.4×10^{-5} cm s^{-1}
 212 or about 2.2 % of saturated hydraulic conductivity of sand) and a theoretical travel time of
 213 the water front of 8h (see Table 2). The initial CT scan of the column was acquired at dry
 214 state. Ten CT scans were performed during the infiltration experiment. Considering the Darcy
 215 velocity and the three-dimensional voxel resolution of 6.3×10^{-3} cm during CT imaging,
 216 the vertical water front travelled across each voxel (of thickness 6.3×10^{-3} cm) in 94 s. An
 217 acquisition time of 25 min roughly corresponds to an uncertainty on the water front position of
 218 16 voxels. This is equivalent to a resolution at the water front edge close to Sammartino et al.
 219 (2012) while achieving a resolution 13 times better anywhere else in the imaged column. The
 220 data volume (1920 images slices of 700 by 700 pixels) was reconstructed using the snapCT
 221 software which allowed for GPU processing acceleration. Iterative construction and adequate

222 filtering reduced reconstruction ring artefacts and beam-hardening effects while preserving
223 the soil core features.

224 2.4 Image Processing and Analysis

225 The reconstructed soil core data volume was provided as a set of 1920 images encoded in
226 16 bits greyscale TIFF images with an effective 14-bit intensity dynamic range. This allows
227 for 65,256 shades of grey to encode material density from dark (corresponding to air or
228 vacuum) to white (for material stopping the penetrating X-rays). The images numbered 0–
229 100 and 1700–1919 were first removed as they mostly contained the top and bottom for
230 flow inlet and outlet located above and below the soil sample. The remaining 1600 images
231 were processed using the ImageJ software (Schneider 2012). They were first cropped and
232 cut to remove all non-porous media elements leading to images of dimension 410 by 410
233 pixels (410 pixels for a width of 2.6 cm, which leads to a spatial resolution of 6.3×10^{-3} cm).
234 Three-dimensional median filtering (Serra 1983) was then applied to remove isolated artefacts
235 typically occupying a volume of less than 3 by 3 by 3 voxels while preserving edges of the
236 larger macropores network.

237 Given the difficulty to use traditional segmentation techniques to separate the macropore
238 system during the infiltration event, a specific technique using subtraction of soil voxels
239 between the dry state and any of the CT volume acquired during the infiltration event is
240 presented in the Sect. 2.5.

241 2.5 Wet Pores Network Thresholding

242 2.5.1 Traditional Segmentation Method

243 One of the most difficult steps to extract water distribution from the CT image is to threshold
244 the grey level corresponding to water. This latter is not straightforward: on the one hand,
245 the presence of water contributes to a spectral shift showed by the close grey levels between
246 water and dry porous media, due to similar material densities (Fig. 2a). On the other hand,
247 the spectral shift due to water contribution varies as a function of water content contained
248 in the investigated porous media volume (Sammartino et al. 2012). Furthermore, the water
249 distribution in the porous media column is never homogeneous along the vertical axe neither
250 in horizontal plans. Therefore, a fixed threshold value cannot be adapted to extract water
251 across all the slices.

252 2.5.2 Subtracted Image Method

253 As the traditional segmentation methods could not be applied to our images, we proposed
254 an alternate method based on the subtraction of CT image acquired at dry state from the one
255 acquired at wet state. This method is used currently in petroleum engineering since the late
256 80's. Withjack (1988) and Akin et al. (2000) determined the porosity by a dual scan at the
257 same location obtained with different fluids saturating the porous medium.

258 Theoretically, the image obtained from subtraction only contains water signal if the fol-
259 lowing conditions are satisfied:

- 260 (1) The soil sample never moved (above the imaging resolution -6.3×10^{-3} cm) during
261 the infiltration experiment and successive scanning sequences;
- 262 (2) The optical configuration of the CT scan never changed during the infiltration experiment;

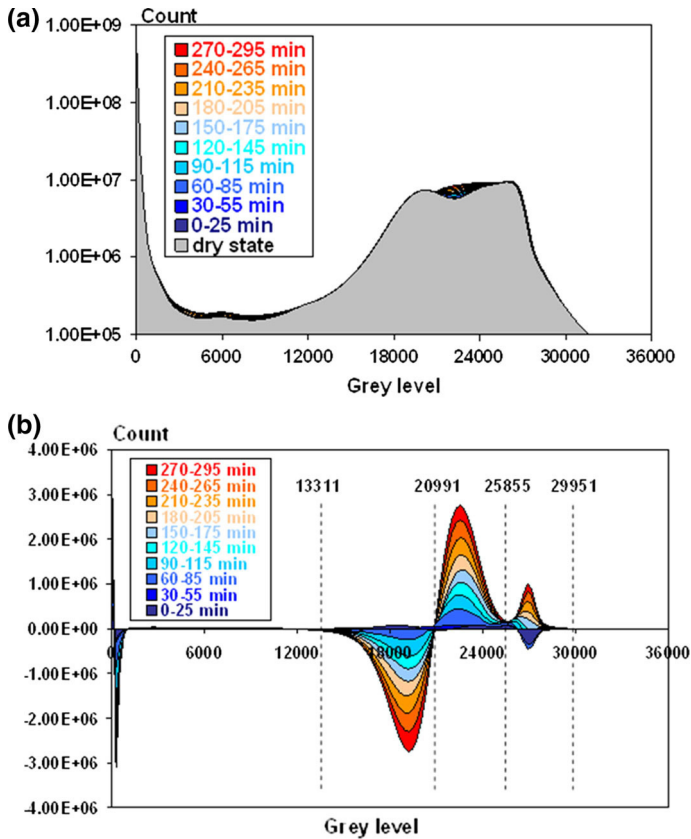


Fig. 2 **a** Grey-level histograms of the whole column (1600 slices) at different states; **b** subtraction of dry histogram from histograms at different time range during infiltration experience

263 (3) The inner soil structure did not change (above the imaging resolution -6.3×10^{-3} cm)
 264 during the infiltration experiment and successive scanning sequences.

265 Both conditions (1) and (3) were verified following the same process: the physical imprints
 266 of the column container (condition 1) and of the sand grains in the soil core (condition 3)
 267 were compared before the infiltration experiment start (first CT scan) and at the saturated
 268 state (last CT scan). The plastic container and the sand grains were isolated out of the
 269 soil core in both first and last CT scan data using traditional segmentation methods (e.g.
 270 histogram segmentation). The resulting binary images for the first and last CT scan data were
 271 subtracted. The resulting difference for the plastic container only displayed isolated pixels
 272 likely representing acquisition noise and/or actual displacement of the studied structure below
 273 the imaging resolution (6.3×10^{-3} cm). This confirmed condition 1. The difference image
 274 of the sand grains exhibited a set of pixels located at the periphery of some of the sand grains.
 275 Overall this did not account for more than a few per cent of the overall sand grains pixels
 276 count and it was considered that condition 3 is loosely verified up to the imaging resolution.
 277 The condition (2) was checked by following the evolution in time of the grey-level histogram
 278 of the glass tube in which the porous media were packed. As the glass tube is completely
 279 inert to its inner content, the grey level of the glass tube contour is invariant whatever the

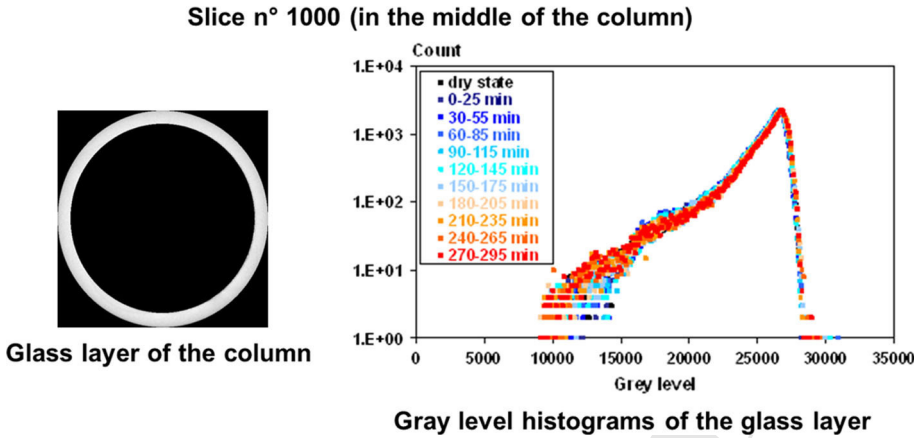


Fig. 3 *Left* glass layer of the column on the slice no. 1000; *Right* glass layer grey-level histograms of the slice no. 1000 at different time range during infiltration experience

280 state of its inner content. As consequence, the only possibility leading to a variant grey level
 281 of the glass tube is the optical configuration change. As the observed grey level of the glass
 282 tube was found constant, the condition (2) is satisfied. An example of the slice no. 1000 (the
 283 slice situated at the middle of the column) is shown in Fig. 3: the grey-level histograms of
 284 this slice displayed the same distribution during the infiltration experience. This validates
 285 our hypothesis.

286 3 Results and Discussions

287 3.1 Hydrodynamic Parameters of the Double-Porosity Media

288 The gravimetric measurement of water content during infiltration is shown in Fig. 4a.
 289 In HN34 sand media, water filled into the inter-aggregate pores until the steady state was
 290 achieved with a water content of $0.29 \text{ cm}^3 \text{ cm}^{-3}$ which is lower than the inter-aggregate
 291 porosity of HN34 sand (0.44). This latter can be explained by the Darcy flow applied of
 292 $6.59 \times 10^{-4} \text{ cm s}^{-1}$ which is lower than the saturated conductivity of HN34 sand and by
 293 the imposed lower boundary condition. In the double-porosity (DP) media, two phases were
 294 observed with different water infiltration kinetics. During the first infiltration phase, the
 295 increasing weight of infiltrated water was rapid and stable; the water content at the end of
 296 the first phase seems to be independent of water flow rates. In the second phase, the water
 297 infiltration was significantly slowed down. We cannot explain the small peak between the
 298 two phases.

299 By knowing the sand/clay spheres quantities (see Table 2), bulk density and porosity of
 300 each media (Table 1), we calculated the inter-aggregate voids volume of the double-porosity
 301 column (i.e. not taking into account the intra-aggregates voids inside the clay spheres). We
 302 found an inter-aggregate porosity of $0.18 \text{ cm}^3 \text{ cm}^{-3}$, whereas the water content at the end of
 303 the first phase was around $0.17\text{--}0.18 \text{ cm}^3 \text{ cm}^{-3}$ whatever the soil column. We can conclude
 304 that for the first phase, the water filled only the inter-aggregate porosity and did not enter
 305 the clay spheres. This water content value also corresponds to the average visible porosity as
 306 determined by CT.

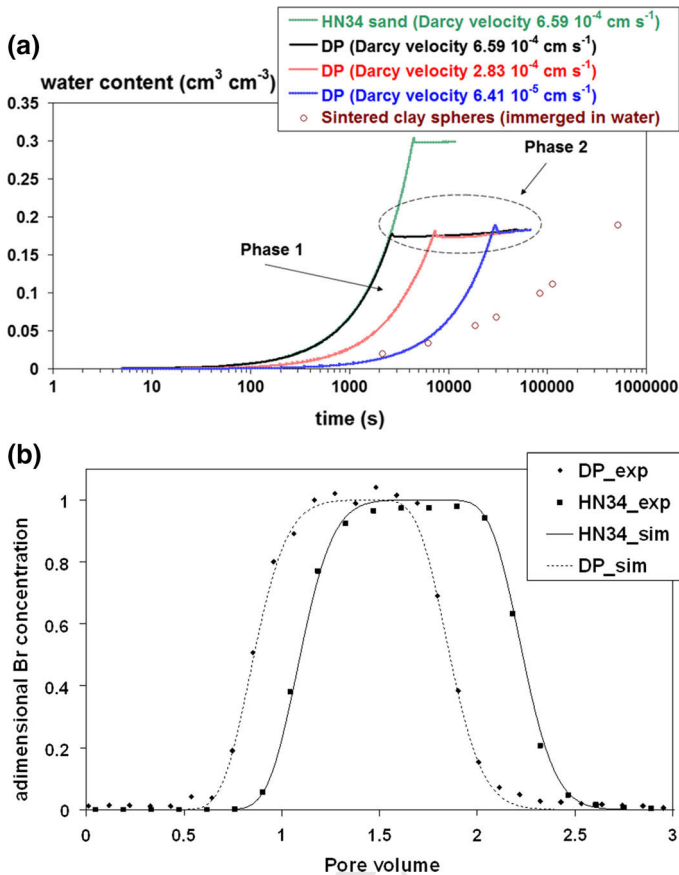


Fig. 4 **a** Gravimetric measurement of water content as function of infiltration time for different columns; **b** experimental (exp) and simulated (sim) breakthrough curves in the double-porosity (DP) and sand (HN34) column, with Darcy velocity of $6.59 \cdot 10^{-4} \text{ cm s}^{-1}$

307 For the second phase, the slow increase in water content in the DP media can be due
 308 to filling of water into the clay spheres, at long infiltration time. By comparison, the water
 309 content in the HN34 sand media which were obtained in the same set-up did not increase
 310 when steady state was achieved. To verify this latter hypothesis, a simple test was performed
 311 by immersing 13 clay spheres in water and weighting them at different time intervals. Water
 312 content evolution with time of the 13 clay spheres is also shown in Fig. 4a. Even immersed
 313 in water, the water infiltration kinetic in clay spheres is slower than the infiltration kinetic in
 314 HN34 sand or DP media. This result shows that the increase in water content observed in the
 315 second phase in the DP media is certainly due to water infiltration inside clay spheres. One
 316 should be noted that this infiltration of water in clay spheres occurred at very large timescale
 317 which is out of our CT experience as described later.

318 To determine the hydrodispersive parameters of the DP media, the breakthrough curve
 319 (BTC) of Br was registered after the gravimetric water content measurement in DP column 1
 320 in which the Darcy flow was $6.59 \cdot 10^{-4} \text{ cm s}^{-1}$. For comparison, another BTC was registered
 321 in HN34 sand column with the same Darcy flow. In permanent regime, the water contents
 322 were 0.188 and $0.29 \text{ cm}^3 \text{cm}^{-3}$ for DP and HN34 sand column respectively. Br transport in

the HN34 sand column was in equilibrium, with a retardation of 1.1, and a dispersivity of 0.07 cm. As observed on Fig. 4b, Br BTC in the DP media goes out earlier than Br in the sand. Supposing that Br retardation was the same in the sand and in the DP media, the equilibrium convection–dispersion equation could not be fitted to the Br BTC in the DP media. By fitting the non-equilibrium convection–dispersion equation, we found a dispersivity of 0.13 cm, a mobile water content ratio of 0.86, and solute exchange rate between mobile and immobile regions of $6.6 \times 10^{-12} \text{ s}^{-1}$. For comparison, Tran Ngoc (2008) found a dispersivity value of 0.69 cm in their DP media under unsaturated conditions ($0.313 \text{ cm}^3 \text{ cm}^{-3}$) to be compared to a dispersivity of 0.044 cm in the sand at a water content of $0.355 \times \text{cm}^3 \text{ cm}^{-3}$ (Sato et al. 2003). Although the water content and the Darcy velocity in our experiment were lower, and knowing that Tran Ngoc worked with a finer sand (HN38, with a mean grain diameter of 0.0162 cm), we found the same increase in dispersivity in the heterogeneous medium compared to the homogeneous medium (Toride et al. 2003).

In our experiment, we applied a pulse input and the shape of BTC in the DP media was slightly dissymmetrical with an early breakthrough of Br compared to one pore volume, while it shows a typical convective/dispersive feature in HN34 sand (Fig. 4b). Bromide transport in the DP media was in physical non-equilibrium, with 14% of the water content not participating in the transport. The exchange between immobile and mobile water is very slow (rate of $6.6 \times 10^{-12} \text{ s}^{-1}$) explaining the nearly symmetrical curve. Tran Ngoc (2008) registered the BTC by applying the water tracer as a step input in homogeneous media (sand) or heterogeneous media (double porosity). They found that the BTC in homogeneous sand was symmetrical, while the BTC in double-porosity media showed non-Fickian characteristics with rapid early breakthrough of the tracer (NaCl) at short times and a drag effect of solute concentration at long time. Furthermore, they also simulated a BTC by assuming that the embedded clay spheres were impermeable; in this case, the breakthrough of tracer concentration was later observed, and the drag effect of solute concentration was reduced even in the presence of clay spheres. They concluded that the early breakthrough and drag effects were due to the presence of porous embedded clay spheres.

Characteristic times were calculated for our DP displacement experiment: resident solute time was 2857 s, whereas the convective time was 2446 s, to be compared to time of exchange between mobile and immobile water zone: $3.9 \times 10^{10} \text{ s}$ and diffusive time: $6.6 \times 10^{10} \text{ s}$. It shows clearly that the main process is the convection during the time of the displacement experiment (total duration of 16,800 s) and that diffusion of water in the clay spheres will happen at longer times. As shown in Table 1, the Ks value of clay spheres used in this work, obtained by XDQ code (Xu et al. 1997), is six times smaller than that of Tran Ngoc (2008). As consequence, the convective transport in the clay spheres is negligible. This led to the nearly symmetrical BTC. According to these macroscopic results, it validates our above results from gravimetric measurements that the water transfer occurred mainly in the pores between sand grains and that the clay spheres were weakly wetted during water transport.

It has to be noted that the Darcy flow applied during infiltration in CT experience was only $6.41 \times 10^{-5} \text{ cm s}^{-1}$ which is 10 times smaller than this applied in BTC measurement, in the aim to slow down water front displacement for CT measurements. As a consequence, the water distribution as well as the water transport properties in the column can be different with these two applied flows. In the work of Tran Ngoc (2008), numerous BTC measurements were performed in homogeneous HN38 sand and heterogeneous double-porosity media, at different Darcy flows under unsaturated and saturated conditions. Whatever the homogeneous or heterogeneous media, they showed increasing early breakthrough and drag effects at saturated state compared to unsaturated states. We might thus have a decrease in immobile water content for lower Darcy flow, such as our infiltration experiment in the CT.

3.2 Images Analysis and Water Distribution Extraction/Determination

3.2.1 Traditional Segmentation Method

Figure 2a shows the original grey-level histograms of the whole column as a function of infiltration time range. Each histogram is the sum of histograms of 1600 slices forming the column and corresponds to the value registered during the acquisition time range (25 min). In order to clarify the band assignments, the histogram at dry state was subtracted to each histogram at different time range during the infiltration (Fig. 2b). As the histograms mathematically (not spatially) refers to grey-level counts of all the voxels summed at the whole column, the difference of histograms between dry state and infiltration at given time range gives insights into the grey-level band assignments, i.e. the counts of a positive peak is equal to the amount of voxels (with unknown spatial coordination), in which the grey level changed from initial state to a given state according to the experiences. In our case, during infiltration (a wetting process), the two positive peaks (positioned at grey-level bands of 20,991–25,855 and 25,855–29,951) are due to the presence of water which leads to spectral shift towards higher grey level in the range of 20,000–30,000. The adjacent negative peak (grey-level band of 13,311–20,991) corresponds to the loss of initial void (air) that was filled by water during infiltration. As well, the signs of these peaks would be inverted if we performed a drying process (not done). Using the corresponding grey-level band of these peaks, the different phases were not so clearly separated when the images were segmented using traditional techniques (e.g. histogram segmentation using the above grey-level bands limits as lower and upper thresholds). Figure 5 shows the slice no. 1000 at wet state (time range 270–295 min), while the whole grey-level distribution is given in Fig. 5a. The grey-level band of 13,311–20,991 (Fig. 5b) which corresponds to pixels representing air also shows a major occupation in the sand, in a clay sphere near the centre of the core. The grey-level band of 20,991–25,855 (Fig. 5c) seems to represent the water in the sand matrix and inside clay spheres. The band of 25,855–29,951 (Fig. 5d) shows the remaining contribution of clay spheres and glass layer.

3.2.2 Subtracted Image Method

The subtracted image method is illustrated in Fig. 6 with the slice no. 1000: Fig. 6a corresponds to the dry image and its grey-level values distribution (presented as a histogram); Fig. 6b corresponds to wet image of the same CT slice and its respective grey-level values distribution. The resulting subtracted image with positive grey levels (Fig. 6c) showed a distinct separated phase with major water contribution in sand and slight contribution in clay spheres. Given their respective density, the water-filled pixels have higher grey-level values than the air/vacuum filled pixels. Pixels which were filled with air in the reference stack (dry state) and are now filled with water at time t exhibits positive grey-level values on the subtracted image. The materials which were optically and geographically invariant during the infiltration lead to the grey level of 0. The subtracted image also showed a range of negative grey levels (Fig. 6d). In [Sammartino et al. \(2012\)](#), it was considered that the range of negative grey values may correspond to voxels where the water was initially present but had left at time t . However, a negative range of grey level does not have a physical sense in our case, as we used an “artificial” porous media initially at the dry state. The only possibility to explain a negative value in our case is that at a given pixel position, the sand grain moved from several micrometres during water infiltration and was replaced by air or water which results in a negative value while image subtraction. The image of negative grey levels only showed an

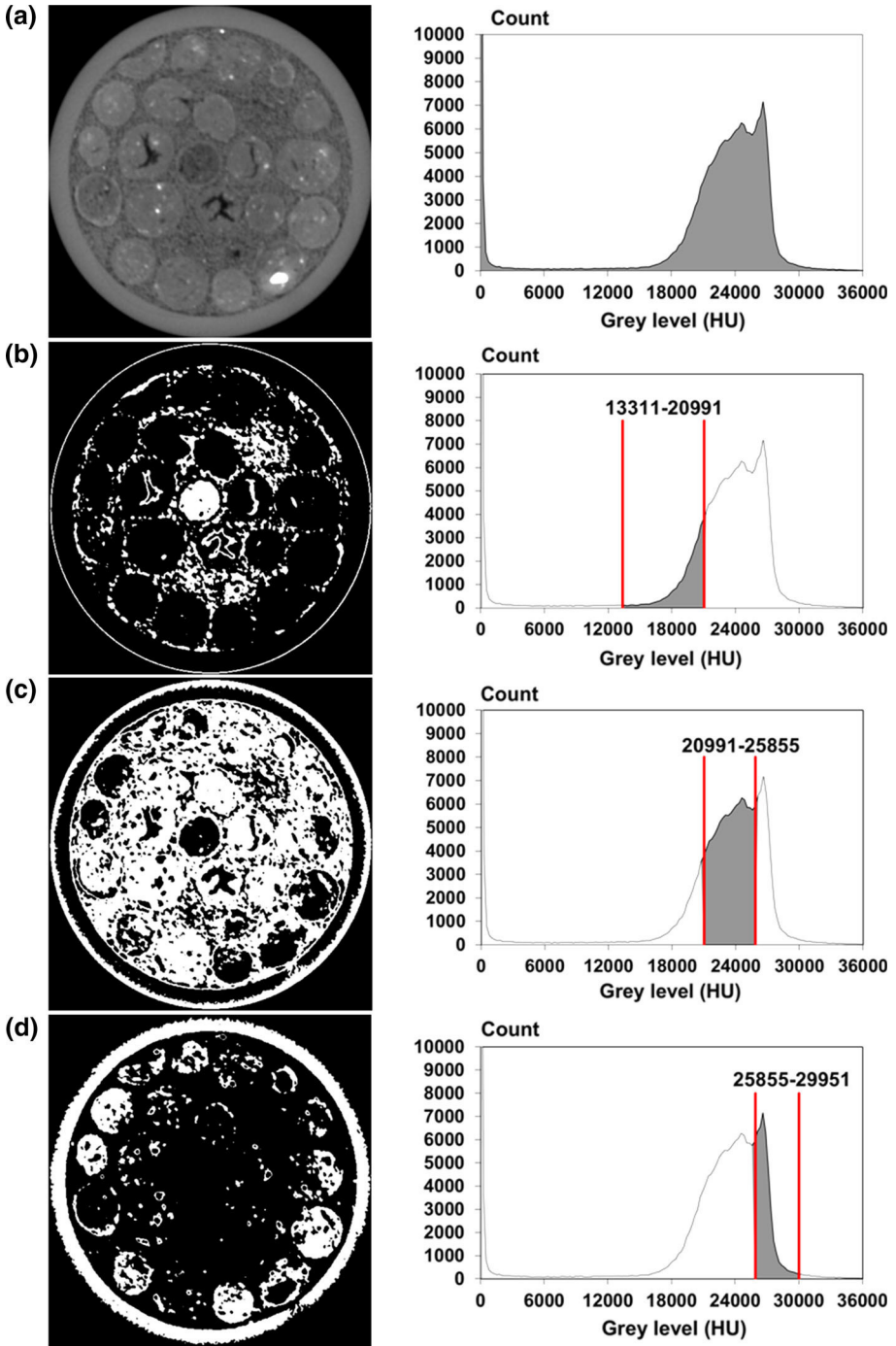


Fig. 5 Image segmentation of the slice no. 1000 at time range 270–295 min of infiltration, with visual images at left and corresponding grey-level band at right for three segmentation ranges: a whole range; b 13,311–20,991; c 20,991–25,855; d 25,855–29,951

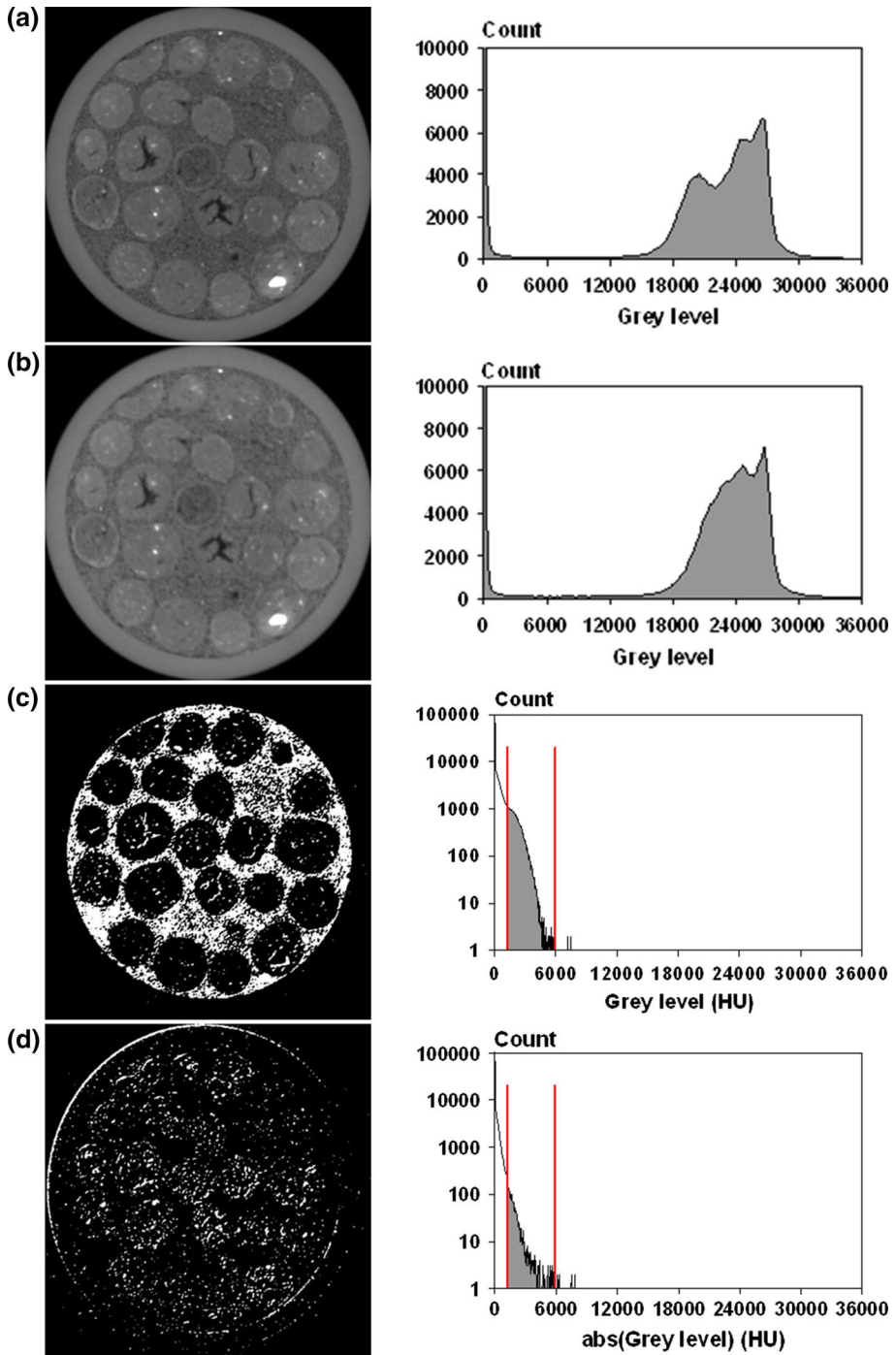


Fig. 6 Example of the slice no. 1000 with visual images at *left* and corresponding *grey level band* at *right* for **a** slice of dry state; **b** slice of wet state at time range 270–295 min; Binary subtracted image with **c** positive grey levels; **d** negative grey levels

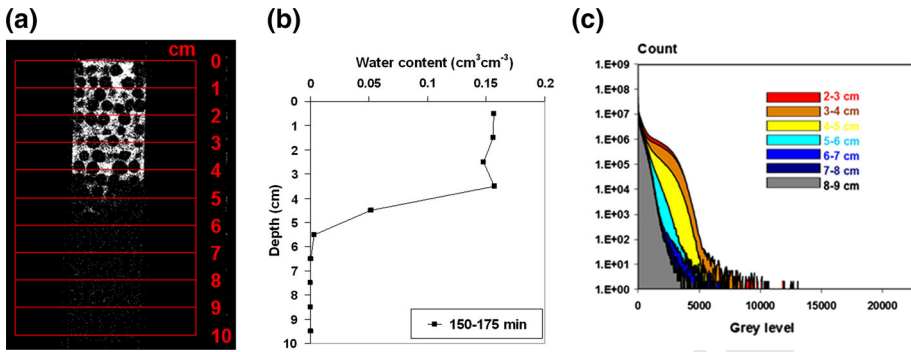


Fig. 7 Example of water content profile obtained with CT images at time range 150–175 min: **a** vertical CT water profile (subtracted image), the void and filled by water volumes are represented by *black* and *white* colours, respectively; **b** water content profile obtained with 3D CT images: each point showed the average water content per layer of 1 cm (160 slice per layer); **c** the histogram sum of 160 slices comprised in each layer of 1 cm thickness

417 opaque mask with low statistic bins count (the range included in red interval, Fig. 6d). We
 418 believe that these negative pixels/voxels may relate to the “diffuse matrix” (in Sammartino
 419 et al. 2012) that is voxels/pixels which were filled by a combination of air and soil at the dry
 420 state and are constituted by a combination of water and soil at time t . This combined with
 421 microdisplacement of the sand grains below the imaging resolution may result in an apparent
 422 voxel grey-level value lower at time t , thus creating subtracted image voxels with negative
 423 pixel values. This is consistent with our hypothesis in condition (3). As a consequence, the
 424 discussion concerning the water transport was rather focused on the image obtained with
 425 positive grey levels. Compared to what was obtained by traditional segmentation method,
 426 we found that the subtracted image method showed much higher image quality, especially
 427 in terms of water distribution.

428 Finally, all the 1600 slices of subtracted image were segmented and converted in binary
 429 format with pixel values 0 and 1 for, respectively, void and water. Considering that all pores
 430 are filled with water above the infiltration front, the threshold for binary image segmentation
 431 was chosen so that the average water content in wet layers of the last scan (at time range of 270–295
 432 min) was close to the theoretical inter-aggregate porosity of the column 3 ($0.181 \text{ cm}^3 \text{ cm}^{-3}$).
 433 Water content of each slice was then calculated as the ratio of water bins count onto the total
 434 bins count of column section. An example is shown in Fig. 7: at the time range of 150–175
 435 min during the infiltration, vertical water profile (Fig. 7b) is calculated from water contents
 436 averaged over 1 cm (160 slices) which is about the height of the periodic layer. The subtracted
 437 CT image profile (Fig. 7a) is also showed for comparison. The water content profile (Fig. 7b)
 438 showed consistent evolution with subtracted CT images (Fig. 7a), i.e. water front lies between
 439 4 and 6 cm in depth and water content drops to 0 below 6 cm. As well, statistical bins account
 440 on the grey-level histograms (Fig. 7c) decreased layer by layer from 0 to 6 cm (the layers of
 441 0–1 and 1–2 cm were not shown because they exhibited the same histogram than the layer
 442 of 2–3 cm) and reached a minimal account below the layer of 6–7 cm.

443 3.3 Evolution of 2D Water Profile and Water Front in 3D

444 With lastly mentioned method, evolution of vertical water profiles in column 3 with time is
 445 shown in Fig. 8 and compared with corresponding CT images. According to the CT images
 446 (Fig. 8 left), sphere voids appeared behind the water front and maintained their void shape

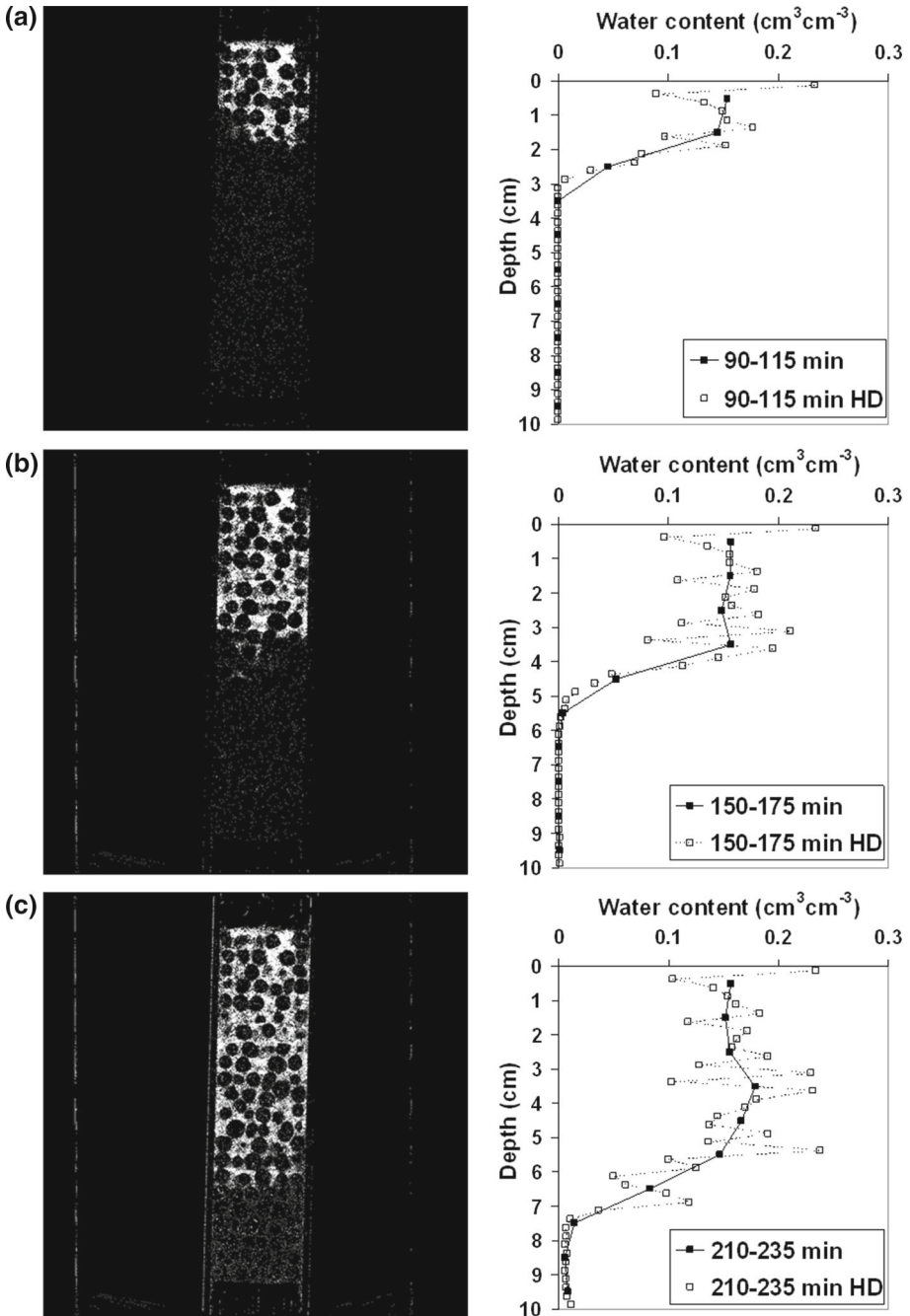


Fig. 8 Left Vertical CT water profiles, the void and filled by water volumes are represented by *black* and *white* colours; Right water content profiles, for the time ranges of **a** 90–115 min, **b** 150–175 min and **c** 210–235 min

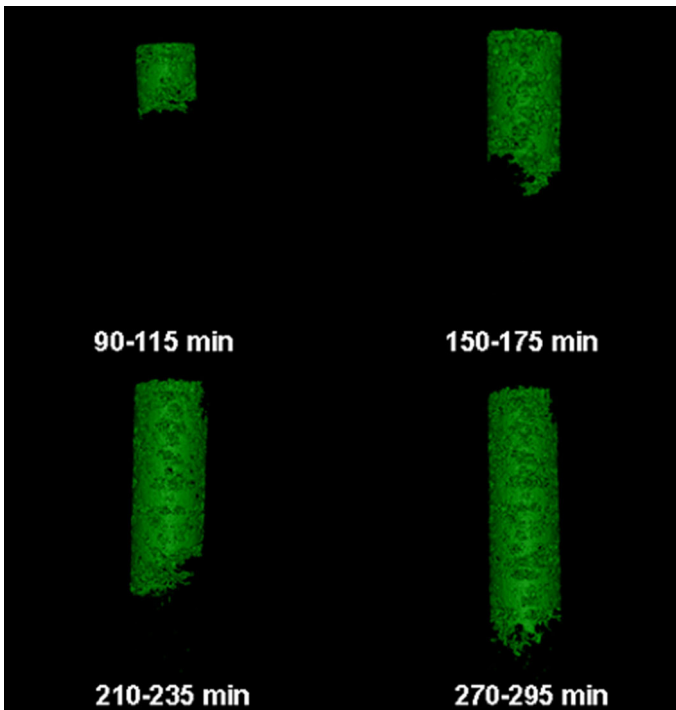


Fig. 9 3D water volume reconstruction at different time ranges of the infiltration

447 along water front advance. These sphere voids correspond logically to clay spheres and
 448 showed that little water filled into clay spheres during infiltration. This is consistent with
 449 what found in gravimetric measurement. On the water content profiles (Fig. 8 right), two
 450 different control volumes are compared. The low resolution corresponds to the average of
 451 water content over around one periodic layer (every 1 cm) and the high resolution (HD) to a
 452 step of 0.25-cm height. The HD profiles showed clearly fluctuating profiles compared to these
 453 of low resolution. This latter can be explained by the sensibility of HD profile associated with
 454 local constitution of sand and clay spheres at different layers. As water hardly filled into clay
 455 spheres, water content is lower in the layers where more clay spheres are present. As well,
 456 while water content is averaged over more slices (low definition), the corresponding water
 457 content is found similar to average inter-aggregate porosity of double-porosity media and the
 458 profiles exhibit less fluctuation. The periodic layer is thus a good representative elementary
 459 volume for water content calculation.

460 By the 3D reconstruction of subtracted images, we noticed that the water front was
 461 heterogeneous (Fig. 9) and is linked to physical non-equilibrium as shown during solute
 462 displacement experiment.

463 **4 Conclusions and Perspectives**

464 In this study, we developed an efficient method to couple images acquisition by computed
 465 tomography technique and water infiltration experiment, in the aim to visualize water distribu-
 466 tion in 4D at submicron scale. In order to overcome the common difficulty in CT technique,

467 i.e. the low temporal resolution vs. to rapid physical phenomena of water transport, we chose
 468 carefully the experimental combination among infiltration speed and relatively high temporal
 469 and spatial resolution CT configuration.

470 By first performing macroscopic measurements in a column made of two medium of con-
 471 trasted hydraulic conductivities (sand and porous clay spheres), we showed that the infiltration
 472 of water into the clay spheres was negligible at the observed time scale. The calculation of
 473 characteristics times show that water transfer into clay spheres is mainly diffusive at times
 474 larger than our infiltration experiment duration.

475 In order to observe water flow at finer spatial scale, we succeeded to follow the water
 476 front displacement by CT imaging, and by a novel image analysis method in soil science,
 477 we could extract water distribution in two and three dimensions. The obtained 2D or 3D
 478 water distribution showed us that little water filled into clay sphere during the observed
 479 time range of infiltration. This is consistent with macroscopic gravimetric measurements.
 480 By averaging the water content over one periodic layer, we could obtain the water content
 481 evolution along the column and determine the depth of the water infiltration front, as observed
 482 in the subtracted binary images. By reconstructing 3D water distribution, we found that the
 483 water front showed a heterogeneous shape which was related to the heterogeneity of the
 484 double-porosity media leading to water transfer in physical non-equilibrium.

485 This work presents an adequate method to study water transport kinetics by CT tech-
 486 nique. However, enhancement of experimental set-up is still needed. The spatial resolution of
 487 6×10^{-3} cm in this work is not high enough to study processes at the pore scale between
 488 sand grains and inside clay spheres. The temporal resolution of 25 min compared to 8-h
 489 infiltration allowed following the water front well, but still showed an uncertainty on the
 490 water front position of 16 voxels or 0.096 cm. To further improve the temporal resolution, we
 491 need higher intensity of the radiation (i.e. higher photon particle amount included in a wave
 492 packet) while keeping low photon energy for high-transmission-coefficient contrast. This
 493 may be realized by grand instrument such as synchrotron facility to image smaller samples
 494 (a few millimetres thick). To improve the spatial resolution, a direct remedy is to use a better
 495 CDD sensor with higher pixel resolution. Lowering carefully the wavelength of the radiation
 496 can provide higher interaction between the radiation and material at small length scale and
 497 thus better spatial resolution. However, a decrease in the wavelength leads to increase in the
 498 photon energy. This has to be adjusted carefully in order to keep a minimal transmission
 499 coefficient contrast.

500 **Acknowledgments** This project and post-doc scholarship for Z. Peng have been funded by a specific grant
 501 awarded by Grenoble Institute of Technology. We thank J.F. Daian for the help in using XDO software. This
 502 project has also received partial funding from the European Union's Horizon 2020 research and innovation
 503 programme under Grant Agreement No. 645717.

504 References

- 505 Akhtar, M.S., Stüben, D., Norra, S., Memon, M.: Soil structure and flow rate-controlled molybdate, arsenate
 506 and chromium(III) transport through field columns. *Geoderma* **161**(3–4), 126–137 (2011)
- 507 Akin, S., Schembre, J.M., Bhat, S.K., Kovscek, A.R.: Spontaneous imbibition characteristics of diatomite. *J.*
 508 *Pet. Sci. Eng.* **25**(3–4), 149–165 (2000)
- 509 Angulo-Jaramillo, R., Vandervaere, J.P., Roullet, S., Thony, J.L., Gaudet, J.P., Vauclin, M.: Field measurement
 510 of soil surface hydraulic properties by disc and ring infiltrimeters—a review and recent developments.
 511 *Soil Till. Res.* **55**(1–2), 1–29 (2000)
- 512 Carminati, A., Kaestner, A., Ippisch, O., Koliji, A., Lehmann, P., Hassanein, R., Vontobel, P., Lehmann, E.,
 513 Laloui, L., Vulliet, L., Flüßler, H.: Water flow between soil aggregates. *Transp. Porous Med.* **68**(2),
 514 219–236 (2007)

- 515 Carminati, A., Kaestner, A., Lehmann, P., Flüher, H.: Unsaturated water flow across soil aggregate contacts.
516 *Adv. Water Resour.* **31**(9), 1221–1232 (2008)
- 517 Dal Ferro, N., Delmas, P., Duwig, C., Simonetti, G., Morari, F.: Coupling X-ray microtomography and mercury
518 intrusion porosimetry to quantify aggregate structures of a cambisol under different fertilisation
519 treatments. *Soil Till. Res.* **119**, 13–21 (2012)
- 520 Desauany, A.: Etude et modélisation de la biosorption des métaux par les bactéries. Application au transfert du
521 cadmium et du zinc, seuls ou en mélange, par *Escherichia coli* et *Cupriavidus metallidurans* en colonnes
522 de sable d'Hostun. PhD of Joseph Fourier university (2011)
- 523 DiCarlo, D.A., Seale, L.D., Ham, K., Willson, C.S.: Tomographic measurements of pore filling at infiltration
524 fronts. *Adv. Water Resour.* **33**(4), 485–492 (2010)
- 525 Elyeznasni, N., Sellami, F., Pot, V., Benoit, P., Vieublé-Gonod, L., Young, I., Peth, S.: Exploration of soil
526 micromorphology to identify coarse-sized OM assemblages in X-ray CT images of undisturbed cultivated
527 soil cores. *Geoderma* **179**, 38–45 (2012)
- 528 Esser, H.G., Carminati, A., Vontobel, P., Lehmann, E.H., Oswald, S.E.: Neutron radiography and tomography
529 of water distribution in the root zone. *J. Plant Nutr. Soil Sci.* **173**(5), 757–764 (2010)
- 530 Heindel, T.J., Gray, J.N., Jensen, T.C.: An X-ray system for visualizing fluid flows. *Flow Meas. Instrum.* **19**(2),
531 67–78 (2008)
- 532 Herman, G.T.: *Fundamentals of Computerized Tomography: Image Reconstruction from Projections*, 2nd edn.
533 Springer Publishing Company Inc., New York (2009)
- 534 Holtham, D.A.L., Matthews, G.P., Scholefield, D.S.: Measurement and simulation of void structure and
535 hydraulic changes caused by root-induced soil structuring under white clover compared to ryegrass.
536 *Geoderma* **142**(1–2), 142–151 (2007)
- 537 Hopmans, J.W., Vogel, T., Koblak, P.D.: X-ray tomography of soil–water distribution in one-step outflow
538 experiments. *Soil Sci. Soc. Am. J.* **56**(2), 355–362 (1992)
- 539 Kneafsey, T.J., Seol, Y., Gupta, A., Tomutsa, L.: Permeability of laboratory-formed methane-hydrate-bearing
540 sand: measurements and observations using X-ray computed tomography. *SPE J.* **16**(1), 78–94 (2011)
- 541 Lewandowska, J., Szymkiewicz, A., Burzynski, K., Vauclin, M.: Modeling of unsaturated water flow in double-
542 porosity soils by the homogenization approach. *Adv. Water Resour.* **27**(3), 283–296 (2004)
- 543 Lewandowska, J., Szymkiewicz, A., Auriault, J.: Upscaling of Richards' equation for soils containing highly
544 conductive inclusions. *Adv. Water Resour.* **28**(11), 1159–1170 (2005)
- 545 Lewandowska, J., Szymkiewicz, A., Gorczewska, W., Vauclin, M.: Infiltration in a double-porosity medium:
546 experiments and comparison with a theoretical model. *Water Resour. Res.* **41**(2), W02022 (2005bis)
- 547 Lewandowska, J., Tran Ngoc, T.D., Vauclin, M., Bertin, H.: Water drainage in double-porosity soils: experi-
548 ments and micro–macro modeling. *J. Geotech. Geoenviron.* **134**(2), 231–243 (2008)
- 549 Lugato, E., Morari, F., Nardi, S., Berti, A., Giardini, L.: Relationship between aggregate pore size distribution
550 and organic–humic carbon in contrasting soils. *Soil Till. Res.* **103**(1), 153–157 (2009)
- 551 Luo, L., Lin, H., Li, S.: Quantification of 3-D soil macropore networks in different soil types and land uses
552 using computed tomography. *J. Hydrol.* **393**, 53–64 (2010)
- 553 Markowicz, A.A.: X-ray physics. In: Van Grieken, R.E., Markowicz, A.A. (eds.) *Handbook of X-Ray Spec-*
554 *trometry*, pp. 1–28. Marcel Dekker, New York (1993)
- 555 Maruyama, T., Tada, A., Iwama, K., Horino, H.: Direct observation of soil water movement through soil
556 macropores using soft X-rays and stereographing. *Soil Sci.* **168**(2), 119–127 (2003)
- 557 Munkholm, L.J., Heck, R.J., Deen, B.: Soil pore characteristics assessed from X-ray micro-Cf derived images
558 and correlations to soil friability. *Geoderma* **181**, 22–29 (2012)
- 559 Sammartino, S., Michel, E., Capowicz, Y.: A novel method to visualize and characterize preferential flow in
560 undisturbed soil cores by using multislice helical CT. *Vadose Zone J.* (2012). doi:[10.2136/vzj2011.0100](https://doi.org/10.2136/vzj2011.0100)
- 561 Sato, T., Tanahashi, H., Loaiciga, H.A.: Solute dispersion in a variably saturated sand. *Water Resour. Res.*
562 **39**(6), 1155–1162 (2003)
- 563 Schjonning, P., Iversen, B.V., Munkholm, L.J., Labouriau, R., Jacobsen, O.H.: Pore characteristics and
564 hydraulic properties of a sandy loam supplied for a century with either animal manure or mineral fertil-
565 izers. *Soil Use Manage.* **21**(3), 265–275 (2005)
- 566 Schaap, J.D., Lehmann, P., Kaestner, A., Vontobel, P., Hassanein, R., Frei, G., de Rooij, G.H., Lehmann,
567 E., Flüher, H.: Measuring the effect of structural connectivity on the water dynamics in heterogeneous
568 porous media using speedy neutron tomography. *Adv. Water Resour.* **31**(9), 1233–1241 (2008)
- 569 Schneider, C.A., Rasband, W.S., Eliceiri, K.W.: NIH Image to ImageJ: 25 years of image analysis. *Nat.*
570 *Methods* **9**(7), 671–675 (2012)
- 571 Serra, J.: *Image Analysis and Mathematical Morphology*. Academic Press, Inc., Orlando (1983)
- 572 Sleutel, S., Cnudde, V., Masschaele, B., Vlassenbroek, J., Dierick, M., Van Hoorebeke, L., Jacobs, P., De
573 Neve, S.: Comparison of different nano- and micro-focus X-ray computed tomography set-ups for the
574 visualization of the soil microstructure and soil organic matter. *Comput. Geosci.* **34**(8), 931–938 (2008)

- 575 Szymkiewicz, A., Lewandowska, J., Angulo-Jaramillo, R., Butlanska, J.: Two-scale modeling of unsaturated
576 water flow in a double-porosity medium under axisymmetric conditions. *Can. Geotech. J.* **45**(2), 238–251
577 (2008)
- 578 Szymkiewicz, A., Lewandowska, J.: Micromechanical approach to unsaturated water flow in structured geo-
579 materials by two-scale computations. *Acta Geotech.* **3**(1), 37–47 (2008)
- 580 Toride, N., Leij, F.J., van Genuchten, M.Th.: *The CXTFIT Code for Estimating Transport Parameters from*
581 *Laboratory or Field Tracer Experiments. Version 2.1.* U.S. Salinity Laboratory, Riverside, California
582 (1999)
- 583 Toride, N., Inoue, M., Leij, F.J.: Hydrodynamic dispersion in an unsaturated dune sand. *Soil Sci. Soc. Am. J.*
584 **67**, 703–712 (2003)
- 585 Tran Ngoc, T.D.: *Transport de solutés dans un milieu à double-porosit  non satur . Mod lisation par*
586 *homog n isation & applications.* PhD of Joseph Fourier university (2008)
- 587 Vasin, M., Lehmann, P., Kaestner, A., Hassanein, R., Nowak, W., Helmig, R., Neuweiler, I.: Drainage in
588 heterogeneous sand columns with different geometric structures. *Adv. Water Resour.* **31**(9), 1205–1220
589 (2008)
- 590 Vogel, H.J., Roth, K.: Moving through scales and flow and transport in soil. *J. Hydrol.* **272**(1–4), 95–106
591 (2003)
- 592 Wildenschild, D., Hopmans, J.W., Rivers, M.L., Kent, A.J.R.: Quantitative analysis of flow processes in a sand
593 using synchrotron-based X-ray microtomography. *Vadose Zone J.* **4**(1), 112–126 (2005)
- 594 Wildenschild, D., Sheppard, A.P.: X-ray imaging and analysis techniques for quantifying pore-scale structure
595 and processes in subsurface porous medium systems. *Adv. Water Resour.* **51**, 217–246 (2013)
- 596 Withjack, E.M.: Computed tomography for rock-property determination and fluid-flow visualization. *Soc. Pet.*
597 *Eng. Form. Eval.* **3**, 696–704 (1988)
- 598 Xu, K., Daian, J.F., Quenard, D.: Multiscale structures to describe porous media. Part II: transport properties
599 and application to test materials. *Transp. Porous Med.* **26**(3), 319–338 (1997)

Journal: 11242
Article: 572

Author Query Form

**Please ensure you fill out your response to the queries raised below
and return this form along with your corrections**

Dear Author

During the process of typesetting your article, the following queries have arisen. Please check your typeset proof carefully against the queries listed below and mark the necessary changes either directly on the proof/online grid or in the 'Author's response' area provided below

Query	Details required	Author's response
1.	Please check the term 'X-Rays Computed Tomography' that has been changed to 'X-ray Computed Tomography' in the article title.	
2.	Please provide significance for superscript b in Table 2.	
3.	Reference Serra (1982) has been changed to Serra (1983), so that this citation matches the list.	
4.	Please provide the year for the phrase 'late 80's' in the sentence 'This method is used currently in petroleum engineering since the late 80's'.	
5.	Please check and confirm that unit "cm ³ cm ⁻³ " repeated in text is correct.	